Journal of Solid State Chemistry **165,** 228–237 (2002)
doi:10.1006/jssc.2002.9492, available online at http://www/idealibrary.com on IDEAL®

The Family of $Ln_2Ti_2S_2O_5$ Compounds (Ln = Nd, Sm, Gd, Tb, Dy, Ho, Er, and Y): Optical Properties

C. Boyer-Candalen,* J. Derouet,† P. Porcher,†,[1] Y. Moëlo,* and A. Meerschaut*

*Institut des Matériaux Jean Rouxel, Laboratoire de Chimie des Solides, UMR 6502 CNRS-Université de Nantes, 2 rue de la Houssinière, BP 32229, 44322 Nantes, France; and †Laboratoire de Chimie Appliquée de l'Etat Solide, ENSCP, UMR 7574 CNRS, 11 rue Pierre et Marie Curie, 75231 Paris, France
E-mail: porcher@idf.ext.jussieu.fr

Received July 31, 2001; in revised form November 16, 2001; accepted December 21, 2001

The optical properties of $Ln_2Ti_2S_2O_5$ compounds (Ln = Nd, Sm, Gd, Tb, Dy, Ho, Er, and Y) have been measured. Diffuse reflectance spectra revealed a strong absorption band above 2 eV, which explains the color of the compounds. Moreover, other bands, with a lower intensity, have been attributed to 4*f*–4*f* rare earth transitions. In the case of neodymium the derived energy level scheme is rich enough to determinate a set of phenomenological crystal field parameters that correctly reproduce the spectrum. These parameters were also calculated from the crystallographic structure, in a good agreement with the experiment. Finally, the paramagnetic susceptibility, well reproduced by the calculation, confirms that the rare earth is in a trivalent state. © 2002 Elsevier Science (USA)

Key Words: **rare earths; oxysulfides; diffuse reflectance; crystal field energy levels and parameters; paramagnetic susceptibility.**

1. INTRODUCTION

A new series of isotypic compounds with the $Ln_2Ti_2S_2O_5$ composition was very recently synthesized (1, 2). The crystal structure type of these semi-transparent compounds with orange brownish colors can be schematically described as the stacking of a rare earth sulfide layer alternating with a titanium oxide one; this gives to the structure a composite 2D character. The fact that layers are of different natures (oxide versus sulfide type) probably results from the large difference in the oxophilicity of the two associated metal atoms (Ln and Ti). Quite systematically, in Ln–Ti oxychalcogenides, titanium atoms adopt an octahedral coordination with preferentially oxygen atoms in their coordination sphere. In these title compounds, charge equilibrium implies the following Ln (+III) and Ti (+IV) oxidation states to counterbalance S (−II) and O (−II); magnetic measurements agree with the presence of Ln^{3+} cations. The orange to brown–orange color of the series of compounds is indicative of a semiconducting behavior, with an absorption band in the highest energy part of the visible optical spectrum.

We report here on some of the optical properties of that family: the diffuse reflectance measurements for most of the $Ln_2Ti_2S_2O_5$ (Ln = Nd, Sm, Gd, Tb, Dy, Ho, Er, and Y), and the absorption spectrum of $Nd_2Ti_2S_2O_5$. In this compound, a transparency window located in the visible part of wavelength range makes it possible to derive a partial energy level scheme for Nd^{3+}. Therefore, an attempt of crystal field calculation can be done, if starting values of the relevant parameters are derived from the crystallographic structure; the aim was also to compare the calculated and experimental values of the magnetic properties of the neodymium derivatives.

2. CRYSTALLOGRAPHIC BACKGROUND

Figures 1a and 1b show the projection of the structure of $Ln_2Ti_2S_2O_5$ compounds that crystallize in the tetragonal symmetry, space group $I4/mmm$ (No 139); unit cell parameters are given in Table 1. The schematic structural description in terms of "separated 2D building blocks" hides in fact strong interlayer connections. Indeed, the Ti atoms are involved in the oxide layer built from a 2D development of double corner-sharing octahedra (Fig. 2a); this part is well representative of the ReO_3 structure type, which means a vacant central site (12-coordinate site) (see Fig. 1b). However, one of the two apical atoms of the Ti octahedra is a sulfur atom, which is also engaged in the sulfide layer. Thus, such a structure cannot be really considered as a composite layered structure. In the same way, the Ln atoms are engaged in the sulfide layer of rock-salt-type structure, or more exactly a distorted {001} slice of NaCl type with a thickness of half the cell edge of fcc NaCl, i.e., a two-atom-thick layer. Thus, these Ln atoms are coordinated by five sulfur atoms in a square pyramidal

[1]To whom correspondence should be addressed.

0022-4596/02 $35.00

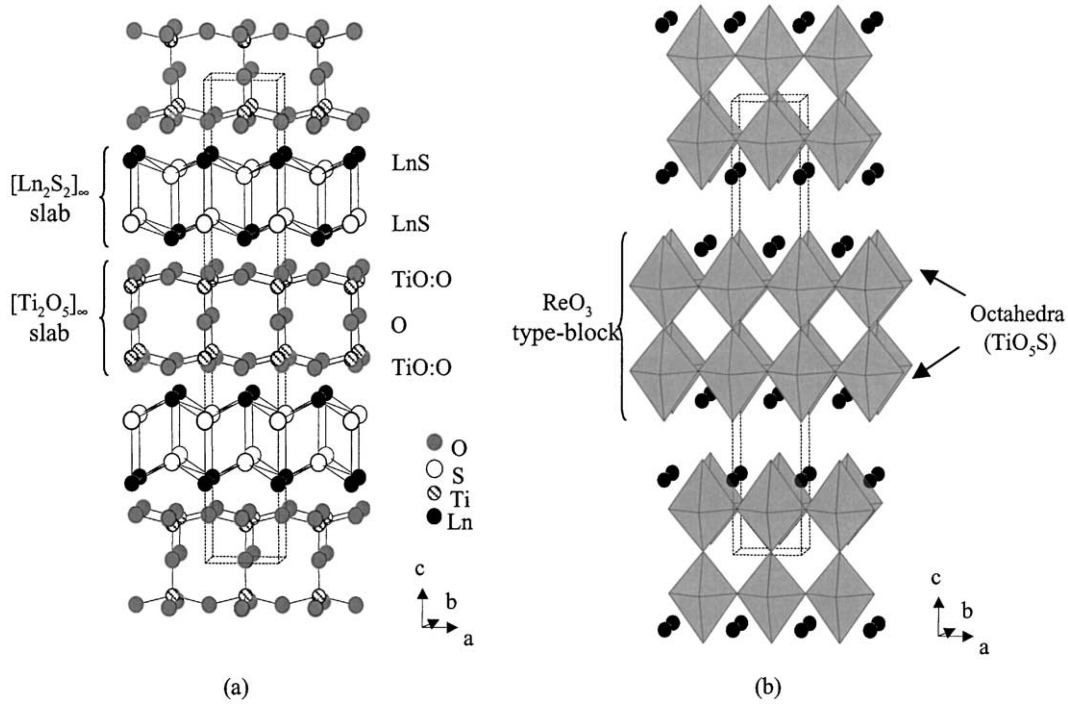

FIG. 1. (a) Stacking of the two kinds of layers along the *c* axis; the rock-salt slab [Ln_2S_2] and the [Ti_2O_2] slab. (b) View down the *b* axis of $Ln_2TiS_2O_5$ showing the double layer of Ti octaedra (ReO_3 type).

arrangement. However, these *Ln* atoms are also coordinated to four oxygen atoms "belonging" to the other oxide layer building block. So, *Ln* atoms are coordinated by nine anions (CN = 9, i.e., five sulfur and four oxygen atoms), corresponding to a tricapped trigonal prismatic coordination (see Fig. 2b), or equivalently to a monocapped square antiprismatic coordination.

The Ln^{3+} ion is located on a C_{4v} point-site symmetry, with the C_4 axis, colinear to the *c* axis, passing through the Ln^{3+} ion. This local environment is very close to that found in the case of NdOCl (3), one representative of a wide series of compounds described on the basis of the $(LnO)_n^{n+}$ complex cation (4). Even the Nd–ligand distances are very similar, which constitutes a feature of considerable help during the simulation of the energy level scheme (5).

TABLE 1
Cell Parameters for the Series of $Ln_2Ti_2S_2O_5$ Compounds

Ln	*a* (Å)	*c* (Å)
Y	3.7710(2)	22.8159(18)
Pr[a]	3.871(1)	23.064(5)
Nd	3.8490(4)	23.019(2)
Sm	3.8205(4)	22.951(4)
Eu	3.8132(5)	22.9194(17)
Gd	3.79864(13)	22.9053(13)
Tb	3.78711(3)	22.8687(17)
Dy	3.7748(2)	22.8334(14)
Ho	3.7678(3)	22.8075(12)
Er	3.7558(4)	22.755(3)

[a] $Pr_2Ti_2O_5S_2$ was characterized by Goga *et al.* (2).

3. DIFFUSE REFLECTANCE MEASUREMENTS

Measurements of diffuse reflectance spectra on synthetic powders were carried out with a Leitz spectrophotometer (MPV-SP), coupled with a Leitz metallographic microscope, working in the visible and close IR range (400 to 800 nm) (2 nm resolution). Diffuse reflectance spectra of $Ln_2Ti_2S_2O_5$ compounds (with *Ln* = Nd, Sm, Gd, Tb, Dy, Ho, Er, and Y) plotted after a Kubelka–Munk transformation are given in Fig. 3. The $F(R_\infty)$ function as defined by Kubelka–Munk (6, 7) relates to the absorption coefficient *K* and the diffusion coefficient *S* of the studied powder. The *K*/*S* ratio depends on the reflectance R_∞ value, at a given wavelength, as long as the particle size is greater than 5 μm:

$$K/S = (1 - R_\infty)^2/2R_\infty = F(R_\infty).$$

The spectra presented in Fig. 3 can be separated into two parts:

(i) a very strong absorption band at high energy. The absorption threshold, corresponding to the crossing point between the base line along the energy axis and the extrapolated line from the linear portion of the absorption

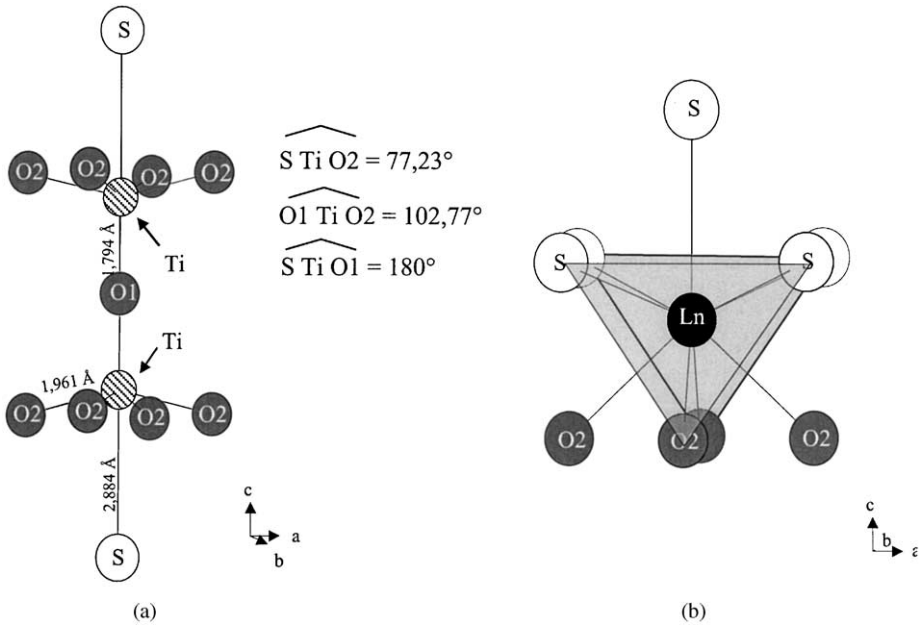

FIG. 2. Atomic environment around Ti (left) and *Ln* (right).

edge in the K/S vs E(eV) plot, is located between 2.00 and 2.14 eV, depending on the rare earth (Table 2). This band corresponds to the transition between the 3*d* vacant band of the titanium and the highest fully occupied 3*p* band of sulfur (8).

(ii) In the case of Nd, Ho, Er, and partially Tb, a series of more resolved bands are observed. They correspond to the 4*f*–4*f* transitions. For the neodymium, these bands are related to the well-known so-called "hypersensitive transitions"; a more complete analysis at low temperature will be presented in Section 4.

The chromatic coordinates (x, y) relative to the standard white light source (illuminant *C*) were determined for each compound; values given in Table 3 are plotted on the C.I.E. chromaticity diagram (Fig. 4). One can observe that dominant wavelengths λ_d of characteristic shades are comparable, i.e., around 588 nm (about 2.1 eV), which corresponds to an orange dominant (hue) color but with purity values (saturation) less than 60% as defined by the ratio BC/BT. A dispersal of points on the BT segment is due, in part, to a different grain size in the powder samples, the decreasing size lowering the purity.

For practical reasons, i.e., the relatively great number of measured energy levels, only the optical properties of Nd^{3+} were studied. Indeed, the study of yttrium (no 4*f* electrons) and the gadolinium derivatives were disregarded because these levels are 4*f* optically nonactive matrices. Studies of Eu^{3+} and Pr^{3+} are generally performed on compounds where these ions are considered as dopant. In contrast the optical studies on Nd^{3+} are numerous in relation with the important role played by that ion in solid state lasers. The abundant literature also results from some peculiarities of this ion characterized by a reasonably sized secular determinant (degeneracy of 364, corresponding to 182 Kramers' doublets). In addition, many crystal field (CF) levels are experimentally positioned by both absorption and emission techniques. This exceptional situation suggests that Nd^{3+} is the most appropriate ion for testing the accuracy of the phenomenological models derived from the theories of atomic spectroscopies (3). The high-quantum efficiency of emission which explains these applications is a direct consequence of the small coupling existing between *f*–*f* electronic excitations and phonons modes.

4. 4*f*–4*f* TRANSITIONS OF $Nd_2Ti_2S_2O_5$

4.1. Experiment

The optical absorption spectra of $Nd_2Ti_2S_2O_5$ were measured on a Varian Cary 5E UV-VIS-NIR spectrophotometer in the transparency area of the material ($<20{,}000\ cm^{-1}$). A refrigerator low-temperature cryostat (Cryophysics) allowed the sample temperature to be varied continuously between 9 and 300 K. Transmission through $Nd_2Ti_2S_2O_5$/KBr pellet (thickness approx. 1 mm) was used as measurement technique. The band width of 0.6 Å used in measurements ensured sufficient resolution of the *f*–*f* absorption lines (Fig. 5).

4.2. Free Ion and Crystal Field Interactions

In the development of a complete Hamiltonian for $4f^N$ configurations, the central-field approximation allows us

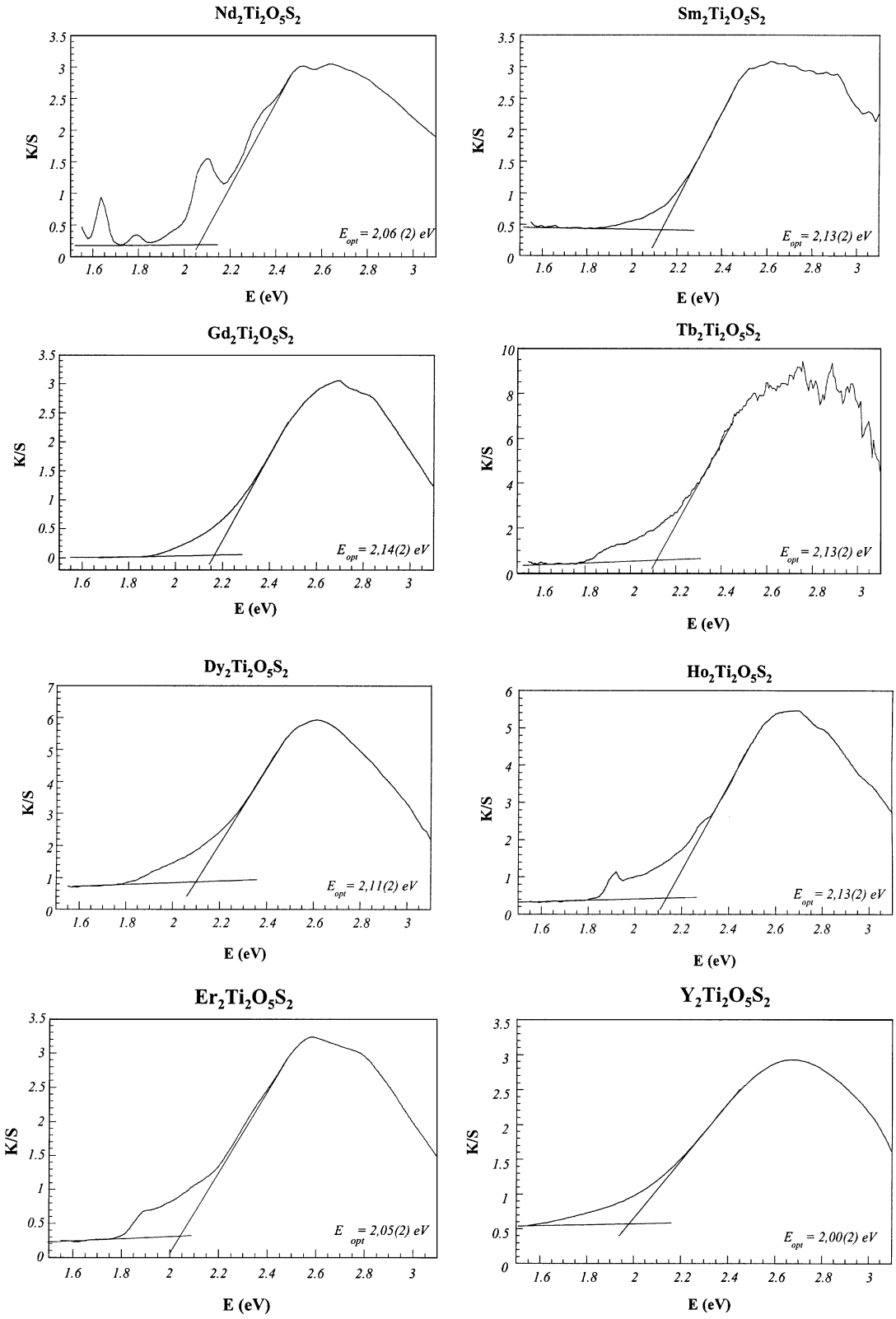

FIG. 3. Diffuse reflectance spectra of $Ln_2TiS_2O_5$, after a Kubelka-Munk transformation ($T = 300$ K).

TABLE 2
Optical Band Gap for the Series of $Ln_2Ti_2S_2O_5$ Compounds

$Ln_2Ti_2S_2O_5$	Y	Nd	Sm	Gd	Tb	Dy	Ho	Er
E (eV)	2.00 (2)	2.06 (2)	2.13 (2)	2.14 (2)	2.13 (2)	2.11 (2)	2.13 (2)	2.05 (2)

to consider separately the Hamiltonian corresponding to the free ion, H_{FI}, and the crystal field Hamiltonian, taking into account the electrostatic interactions of the f electrons with the ions of the crystalline lattice, H_{CF}. This description is only an analytical procedure, because the final treatment includes together all elementary interactions in the secular determinant. The interactions primarily responsible for the free ion structure can be written as (9)

$$H_{FI} = H_0 + \sum_{k=0,1,2,3} E_k e^k + \zeta_{4f} A_{SO} + \alpha L(L+1) + \beta G(G_2) + \gamma G(R_7) + \sum_{\substack{\lambda=2,3,4,\\ 6,7,8}} T^{\lambda} t_{\lambda} + \sum_{k=0,2,4} M^k m_k + \sum_{i=2,4,6} P^i p_i.$$

In this expression, H_0 is for the spherically symmetric one-electron term of the Hamiltonian. The Racah parameters E_k and the spin–orbit coupling interaction $\zeta_{4f}A_{SO}$ correspond to the electrostatic repulsion between equivalent f electrons and the coupling that results from the interaction between the spin magnetic moment of the electron and the magnetic field created by the movement of the electron around the nucleus, respectively. ζ_{4f} is the spin–orbit coupling constant. for configurations of two or more equivalent electrons the two-body interactions are considered with the Trees parameters α, β, and γ associated with the angular moment L and with the Casimir operators G for the groups G_2 and R_7, respectively. Judd parameters T^{λ} account for nonnegligible three-body interactions for configurations having more than two electrons. Magnetically correlated corrections such as spin–spin and spin–other–orbit interactions can be simulated through the Marvin integrals (M^k-parameters). Finally, the electrostatically correlated spin–orbit interactions are described by the P^i integrals.

TABLE 3
Chromatic Coordinates for $Ln_2Ti_2S_2O_5$ Compounds

Compound	x	y
$Y_2Ti_2O_5S_2$	0.373	0.350
$Nd_2Ti_2O_5S_2$	0.397	0.348
$Sm_2Ti_2O_5S_2$	0.408	0.369
$Gd_2Ti_2O_5S_2$	0.444	0.378
$Tb_2Ti_2O_5S_2$	0.4387	0.378
$Dy_2Ti_2O_5S_2$	0.401	0.357
$Ho_2Ti_2O_5S_2$	0.414	0.373
$Er_2Ti_2O_5S_2$	0.390	0.355

Following the Wybourne's formalism (10), H_{CF} is expressed as a sum of products of spherical harmonics and *c*rystal *f*ield *p*arameters, cfp's,

$$H_{CF} = \sum_{k=2}^{4,6} \sum_{q=0}^{k} [B_q^k (C_q^k + (-1)^q C_{-q}^k) + i S_q^k (C_q^k - (-1)^q C_{-q}^k)].$$

The number of the non zero B_q^k and S_q^k phenomenological cfps depends on the crystallographic point-site symmetry of the lanthanide ion. For the C_{4v} symmetry of the Nd^{3+} site in $Nd_2Ti_2S_2O_5$, the serial development of the crystal field potential involves only five real cfp's:

$$H_{CF}(C_{4v}) = B_0^2 C_0^2 + B_0^4 C_0^4 + B_4^4 (C_4^4 + C_{-4}^4) + B_0^6 C_0^6 + B_4^6 (C_4^6 + C_{-4}^6).$$

4.3. The Simple Overlap Model

The *s*imple *o*verlap *m*odel (SOM) has been developed by Malta (11). It has been successfully applied to reproduce the phenomenological cfp's for a great number of lanthanides as well as for some 3d element compounds (12–15). In this model, the cfp's are calculated from the atomic positions in the structure and are written as

$$B_q^k = \rho \left(\frac{2}{1 \pm \rho} \right)^{k+1} A_q^k \langle r^k \rangle.$$

In this expression A_q^k is the lattice sum (16) of neighbors belonging to the first coordination sphere associated with a charge factor g, $\langle r^k \rangle$ are the radial integrals (17), and ρ is the overlap between the $4f$ orbitals of the central ion and the s and p orbitals of the ligand, the value of which varies as a function of the metal–ligand distance R, according to an exponential law $\rho = \rho_0 (R/R_0)^{3.5}$ (18), R_0 being the shortest metal–ligand distance. The $\pm$sign characterizes the displacement of the charge barycenter from the metal–ligand mid distance; the minus sign is applied when $r_{metal} < r_{ligand}$ (12, 19). The overlap integral ρ is comprised between 0.05 and 0.08 for the $4f$ electrons (5, 10). In the present case, due to the great structural analogy with oxysalts, we retain the values previously chosen for

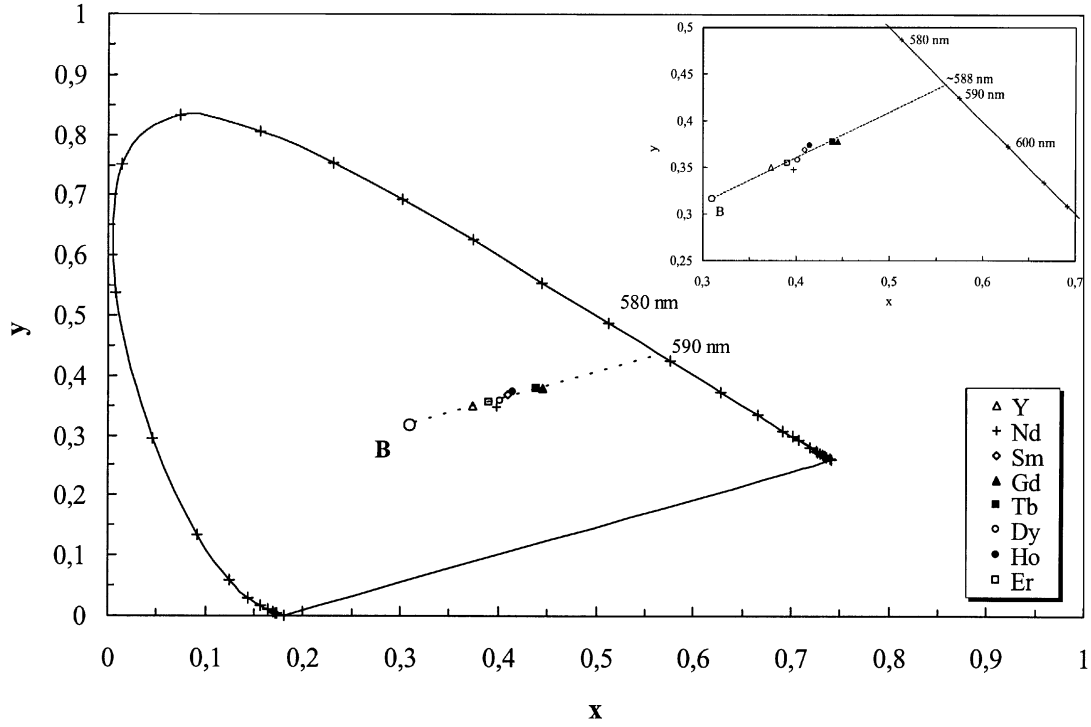

FIG. 4. Chromaticity diagram of $Ln_2TiS_2O_5$.

neodymium oxysulfide, namely $\rho = 0.05$, $g_{O1} = g_{O2} = -0.8$, and $g_s = -2.0$ (15).

The SOM, in which an aspect of the chemical bonding is taken into account, may be regarded as a starting point for carrying out practical crystal field calculations. The determined B_q^k values are introduced for the diagonalization of the secular determinant of the $4f^3$ configuration. It is also useful to introduce the total ligand crystal field strength parameter S (21), which makes it possible to compare different ligands:

$$S = \left[\frac{1}{3}\sum_{k=2,4,6}\frac{1}{2k+1}\sum_{q=-k}^{q=+k}(B_q^k)^2\right]^{1/2}.$$

4.4. Simulation of the $Nd_2Ti_2S_2O_5$ Energy Level Scheme

The analysis of optical data for lanthanide ions with low point-group symmetries or with a reduced number of energy levels is a well-known problem (22, 23). The difficulty arises from the very large number of adjustable parameters required to fit the experimental data with a total Hamiltonian. It is generally accepted that nonlinear least-square fits are unreliable, and several minima indistinguishable from one another insofar as the quality of the fit is concerned may exist. Theoretical constraints can alleviate these difficulties. The free-ion parameters will not vary much for a lanthanide ion in different systems, and can be taken from the literature (9). In contrast, the cfp's show a large variation depending on the host crystal. However, the use of semi-empirically calculated cfp's as starting values in the simulation procedure is helpful. The starting values of cfp's retained here are those deduced from the SOM.

It should be also pointed out that in the present case neither correlated cfp's nor the explicit inclusion of more excited shells will be considered in the simulation. Besides, the great number of parameters introduced force us to be particularly careful on the meaning of the values obtained. For this reason, depending on the observed energy levels and on their sensibility to a given parameter, some of the parameters can be fixed to standard values, corresponding to those calculated or to those found in a matrix yielding a richer information. Among them, γ and Judd parameters, T^{λ}, will be fixed since there are only few levels on which their effects have really importance and because of the reduced number of experimental levels. The fixed values are naturally those previously determined in NdOCl, whose energy level scheme, as well as the geometry of the first coordination sphere, is close to that of $Nd_2Ti_2S_2O_5$ (see Fig. 2b). M^k and P^i cannot be freely varied, and they are always maintained in standard and/or related ratios, which can be the pseudo-relativistic Hartree–Fock calculated ones, $M^2/M^0 = 0.5582$, $M^4/M^0 = 0.3785$, $P^4/P^2 = 0.6667$, and $P^6/P^2 = 0.4899$ (24), or more or less

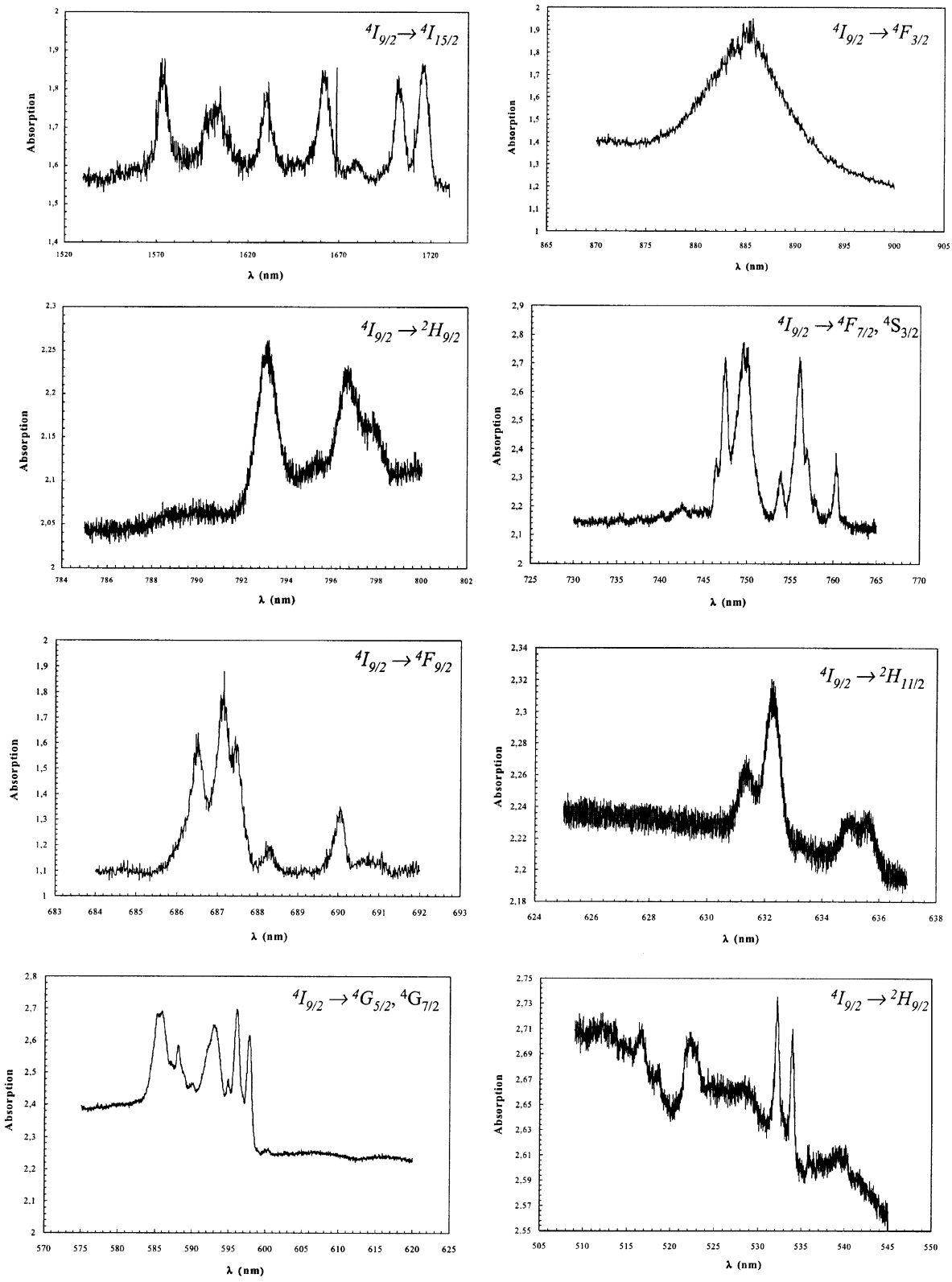

FIG. 5. Detailed absorption spectrum of $Nd_2TiS_2O_5$ at 15 K.

adapted ones, namely $P^4/P^2 = 0.75$ and $P^6/P^2 = 0.50$ (6) or $M^2/M^0 = 0.56$, $M^4/M^0 = 0.31$, $P^4/P^2 = 0.50$, and $P^6/P^2 = 0.10$ (25) (Table 4).

The correct procedure for the simulation of the energy level scheme of Nd^{3+} involves the simultaneous treatment of both the free-ion and crystal field effects using the untruncated basis set of wave functions. The best fit of parameters was obtained by the least-squares refinement between the observed and calculated energy level values through a minimization of the root-mean-square (rms) function $\sigma = [\sum(\Delta_i)^2/(n-p)]^{1/2}$, where Δ_i is the difference between the observed and calculated energies, n is the number of levels, and p is the number of parameters freely varied. In the present case, due to the reduced number of levels, the residue $\sum(\Delta_i)^2$ and the mean deviation $[\sum(\Delta_i)^2/n]^2$ are also considered (Table 5).

TABLE 4
Free Ion and Crystal Field Parameters for $Nd_2Ti_2O_5S_2$

Parameter	Phenomenological	Starting values
E^0	23049.5	23.082
E^1	4603.21	4859
E^2	21.69	22.40
E^3	466.94	490.25
α	18.29	20.96
β	−669.0	692
γ	[1791]	1791
T^2	[398]	398
T^3	[32]	32
T^4	[75]	75
T^6	[−240]	−240
T^7	[296]	296
T^8	[330]	330
ζ	860.5	862.6
M^0	[2.00]	2.00
M^2	[1.13]	1.13
M^4	[0.75]	0.75
P^2	[300]	300
P^4	[225]	225
P^6	[150]	150
B_0^2	−208	−138
B_0^4	−832	−748
B_4^4	−115	−58
B_0^6	499	409
B_4^6	1081	1086
S_2	208.0	138.0
S_4	282.6	250.8
S_6	446.0	440.8
S	327.6	303.5
Number of exp. levels	35	
Residue	7234	
Mean deviation	14.4	
Root mean square deviation	17.7	

Note. Values in cm^{-1} (except the residue in cm^{-2} units).
The strength parameters S_k are defined in the text.
Values in brackets are not varied in the simulation
The starting values are determined as follows:
(i) free ion parameters (except M^k, P^k) from NdOCl and
(ii) crystal field parameters calculated from the SOM.

The simulation of schemes of crystal field energy levels was performed by the programs REEL and IMAGE (26).

4.5. Results of the Simulation

The experimental energy scheme is relatively poor:only 35 out of the 182 levels allowed in the $4f^3$ configuration (Table 5). It is due to the self-absorption of the matrix, the edge of which is located at about 20,000 cm^{-1} (approx. 2.5 eV). This is why some parameters are fixed to the values found in the structurally closed NdOCl. When the number of experimental levels is compared to the number of parameters, the rms standard deviation is not very good, but the residues show that the simulation is very satisfying. Consequently, we can assume that the nonobserved part of the energy levels sequence is close to the calculated values. It is also noteworthy that the phenomenological cfp's are very closed to the SOM calculated values, both globally (through the strength parameters S_k and S) and individually. We could even say that the SOM model is an excellent semi-empirical determination of the cfp's in that case (Table 4).

5. PARAMAGNETIC SUSCEPTIBILITY

The magnetic measurements were performed on powdered samples by a SQUID magnetometer between liquid helium and room temperature. Both zero–field–cooled and field–cooled modes were considered. The gross magnetization is converted into magnetic susceptibility after subtraction of the sample holder contribution and of the intrinsic molecular diamagnetism, calculated from the standard atomic values.

According to Van Vleck (27), the paramagnetic susceptibility χ and its evolution vs temperature is written in the perturbation theory frame as

$$\chi = \frac{N\beta^2}{\sum_i \exp -\left(\frac{E_i^{(0)}}{kT}\right)} \sum_i \left[\frac{(\varepsilon_j^{(1)})^2}{kT} - 2\varepsilon_j^{(2)}\right] \exp -\left(\frac{E_i^{(0)}}{kT}\right)$$

$$\varepsilon_i^{(1)} = \langle \Psi_i | (\mathbf{L} + g_e \mathbf{S}).\mathbf{u} | \Psi_i \rangle$$

$$\varepsilon_i^{(2)} = \sum_{\substack{j \\ E_i^{(0)} \neq E_j^{(0)}}} \frac{[\langle \Psi_i (\mathbf{L} + g_e \mathbf{S}).\mathbf{u} | \Psi_j \rangle]^2}{E_i^{(0)} - E_j^{(0)}}.$$

In these expressions, N is the Avogadro number, k the Boltzmann constant, μ_B the Bohr magneton, and $g_e = 2.0023$. The wave functions ψ_i and ψ_j are the eigenfunctions of the Hamiltonian, unperturbed by the magnetic field, corresponding to the eigenvalues $E_i^{(0)}$, $E_j^{(0)}$. $\mathbf{u}$ is a unit vector describing the three components of the

TABLE 5
Experimental and Calculated Energy Levels (in Part) for $Nd_2Ti_2O_5S_2$

Exp	Calc	Delta	Level	Exp	Calc	Delta	Level
0	8	−8	$^4I_{9/2}$	—	15,764	—	$^2H2_{11/2}$
—	86	—		—	15,766	—	
—	226	—		15,811	15,814	−3	
—	262	—		—	15,817	—	
—	461	—		16,745	16,732	13	$^4G_{5/2}$
—	1,972	—	$^4I_{11/2}$	16,754	16,756	−2	
—	2,007	—		16,863	16,874	−11	
—	2,028	—		17,020	17,046	−26	$^4G_{7/2}$
—	2,029	—		17,066	17,089	−23	
—	2,115	—		—	17,117	—	
—	2,159	—		17,186	17,135	51	
—	3,884	—	$^4I_{13/2}$	18,640	18,672	−32	
—	3,919	—		18,744	18,742	2	
—	3,946	—		18,778	18,773	5	
—	3,947	—		—	18,809	—	
—	4,064	—		—	19,062	—	$^4G_{9/2}$
—	4,087	—		—	19,092	—	
—	4,135	—		—	19,106	—	
5,755	5,756	−1	$^4I_{15/2}$	19,124	19,124	0	
5,795	5,784	11		19,138	19,127	11	
5,927	5,918	9		19,167	19,166	1	$^2K_{13/2}$
5,932	5,935	−3		—	19,186	—	
6,123	6,130	−7		—	19,208	—	
6,176	6,182	−6		—	19,220	—	
6,248	6,246	2		—	19,260	—	
6,340	6,343	−3		—	19,286	—	
11,293	11,297	−4	$^4F_{3/2}$	—	19,403	—	
11,313	11,325	−12		—	20,642	—	$^2D_{13/2}$
—	12,298	—	$^4F_{5/2}$	—	20,665	—	
—	12,321	—		—	20,726	—	$^4G_{11/2}$
—	12,356	—		—	20,742	—	$^2G_{19/2}$
—	12,399	—	$^2H2_{9/2}$	—	20,795	—	
12,509	12,493	16		—	20,813	—	
12,517	12,505	12		—	20,827	—	
—	12,627	—		—	20,907	—	$^4G_{11/2}$
12,650	12,644	6		—	20,992	—	
13,225	13,208	17	$^4F_{7/2}$	—	21,052	—	
13,262	13,251	11		—	21,082	—	
—	13,358	—	$^4S_{3/2}$	—	21,094	—	
—	13,368	—		—	21,121	—	$^2K_{15/2}$
13,379	13,388	−9	$^4F_{7/2}$	—	21,137	—	
—	13,392	—		—	21,162	—	$^4G_{11/2}$
—	14,501	—	$^4F_{9/2}$	—	21,186	—	$^2K_{15/2}$
14,534	14,516	18		—	21,198	—	
14,544	14,552	−8		—	21,204	—	
—	14,566	—		—	21,231	—	
14,583	14,592	−9		—	21,271	—	
15,733	15,738	−5	$^2H2_{11/2}$	—	21,332	—	
15,746	15,754	−8		—	22,730	—	$^2P_{1/2}$

magnetic dipole tensor, related to the three susceptibilities χ_x, χ_y, and χ_z (or $\chi_\parallel$ and $\chi_\perp$ for an axial symmetry). In the case of powdered compounds it is more convenient to consider the mean susceptibility

$$\chi_{Av} = (\chi_x + \chi_y + \chi_z)/3.$$

The wave functions are directly deduced from the diagonalization of the secular determinant. Consequently, this calculation does not involve more parameters. Figure 6 shows the comparison between experiment and calculation. The agreement is satisfying, although a small deviation is observed in the lower and the higher range of the

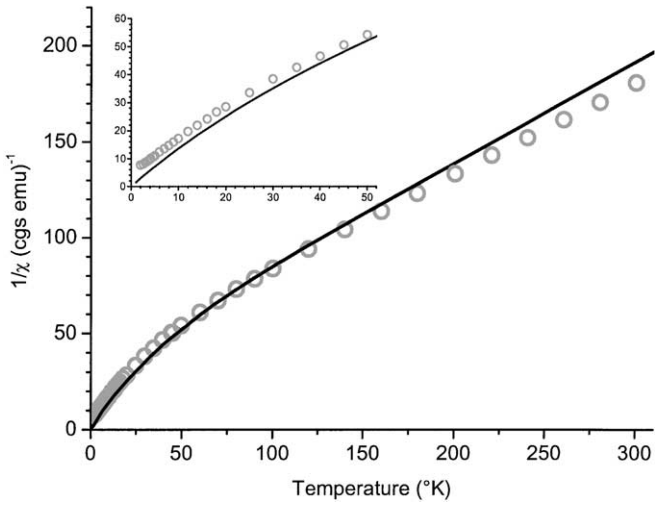

FIG. 6. Experimental and calculated paramagnetic susceptibility of $Nd_2TiS_2O_5$ vs temperature.

temperature measurement scale. It confirms that the rare earth is purely trivalent.

ACKNOWLEDGMENTS

The authors thank Dr A. Lafond for magnetic measurements.

REFERENCES

1. C. Boyer, C. Deudon, and A. Meerschaut, *Comp. Rend. Acad. Sci. Paris 2 sér. IIc*, 93–99 (1999).
2. M. Goga, R. Seshadri, V. Ksenofontov, P. Gütlich, and W. Tremel, *Chem. Comm.* 979–980 (1999).
3. L. Beaury, J. Derouet, and P. Porcher, *J. Alloys Compd.* **225,** 28 (1995); L. Beaury, Ph.D. thesis. Université de Paris-Sud, Orsay, France, 1988.
4. P. Caro, *J. Less Common Met.* **16,** 367 (1978).
5. P. Porcher and P. Caro, *J. Less Common Met.* **83,** 151 (1983).
6. W. W. Wendlandt and H. G. Hecht, "Reflectance Spectroscopy." Interscience New York, 1966.
7. B. Cervelle, A. Bédidi, and N. Flay, *in* "Diffuse Reflectance Properties of Mineral Bearing Surfaces," pp. 35–53. Editions ESKA, Paris, 1996.
8. C. Boyer, thesis dissertation. University of Nantes, 2000.
9. W. T. Carnall, G. L. Goodman, K. Rajnak, and R. S. Rana, *J. Chem. Phys.* **90,** 3443 (1989).
10. B. G. Wybourne, "Spectroscopic Properties of Rare Earths." Wiley–Interscience, New York, 1965.
11. O. L. Malta, *Chem. Phys. Lett.* **87,** 27 (1982); *Chem. Phys. Lett.* **88,** 353 (1982).
12. O. L. Malta and G. F. De Sa, *Quim. Nova (Brazil)* **6,** 123 (1983).
13. O. L. Malta, S. L. J. Ribeiro, M. Faucher, and P. Porcher, *J. Phys. Chem. Solids* **52,** 587 (1991).
14. J. Derouet, L. Beaury, P. Porcher, R. Olazcuaga, J. M. Dance, G. Leflem, M. El Bouari, and A. El Jazouli, *J. Solid State Chem.* **143,** 224 (1999); **143,** 230 (1999).
15. P. Porcher, M. Couto Dos Santos, and O. L Malta, *Phys. Chem. Chem. Phys.* **1,** 397 (1999).
16. C. A. Morrison and R. P. Leavitt, *in* "Handbook on the Physics and Chemistry of Rare Earths," (K. A. Gschneidner, Jr. and L. Eyring, Eds.), Vol. 5, Chap. 46, p. 461. North-Holland, Amsterdam, 1982.
17. A. J. Freeman and J. P. Desclaux, *J. Magn. Magn. Mater.* **12,** 11 (1979).
18. C. K. Jorgensen, "*Modern Aspects of Ligand Field Theory*." North-Holland, Amsterdam, 1971.
19. G. P. Barnett, M. C. Pires Costa, and R. Ferreira, *Chem. Phys. Lett.* **25,** 49 (1974).
20. G. Burns, *J. Chem. Phys.* **42,** 377 (1965).
21. N. C. Chang, J. B. Gruber, R. P. Leavitt, and C. A. Morrison, *J. Chem. Phys.* **76,** 3877 (1982).
22. C. A. Morrison and R. P. Leavitt, *in* "Handbook on the Physics and Chemistry of Rare Earths" (K. A. Gschneidner, Jr. and L. Eyring, Eds.), Vol. 5, p. 461. North-Holland, Amsterdam, 1982.
23. C. Görller-Walrand and K. Binnemans, *in* "Handbook on the Physics and Chemistry of Rare Earths" (K. A. Gschneidner, Jr., and L. Eyring, Eds.) Vol. 23, p. 121. North-Holland, Amsterdam, 1996.
24. G. M. Copland, D. J. Newman, and C. D. Taylor, *J. Phys. B: Atom. Molec. Physc.* **4,** 1388 (1989).
25. H. M. Crosswhite and H. Crosswhite, *J. Opt. Soc. Am.* **1,** 246 (1984).
26. P. Porcher, Fortran routines REEL and IMAGE for simulation of d^N and f^N configurations involving real and complex crystal-field parameters, 1989, unpublished.
27. J. H. Van Vleck, *J. Appl. Phys.* **39,** 365 (1968).